Finite element simulation of ICRF wave heating of core and edge plasmas in EAST

Hua Yang [1], *Lihua* Zheng[2*], *Xinjun* Zhang[1], and *Wei* Zhang[1]

[1]Insititute of Plasma Physics, Chinese Academy of Sciences, Hefei, Anhui, China
[2]University of Science and Technology of China, Hefei, Anhui, China

Abstract. In recent years, simulations using the finite element method (FEM) have been conducted to study ion cyclotron resonance heating (ICRH) in the EAST tokamak (including SOL plasma). This paper improves the previous FEM for solving the perpendicular wavenumber [*Nucl. Fusion.* 62. 7 076032 (2022)], aiming to correct the local deviation in solving the perpendicular wavenumber of cold plasma fast waves. Results show that ion cyclotron resonance heating of the minority ion H dominates energy absorption in the plasma core. The power absorption characteristics of ICRF waves are consistent with previous findings, with potential errors possibly caused by fast wave reflection on the high-field side. These results may provide a reference for future ICRF heating experiments and contribute to experimental optimization through program optimization.

1 Introduction

Ion Cyclotron Resonance Heating (ICRH) is a technique employed for plasma heating in Tokamak fusion reactors. The fundamental principle of ICRH is that by emitting radiofrequency (RF) waves that match the cyclotron frequency of the ions in the plasma, the ions absorb energy directly and undergo heating [1-3]. This heating method is critical for achieving the high-temperature plasma necessary for fusion reactions, as it enables direct heating of ions, eliminating the need for indirect heating of electrons. With the advancement of technology, ICRH systems have been capable of realizing power coupling at the multi-megawatt level and have been widely applied in large, medium, and small tokamaks worldwide [4]. The accumulation of experience in the design and operation of ICRH systems provides an important physical foundation and technical support for the International Thermonuclear Experimental Fusion Reactor (ITER). In ITER, the application of ICRH extends beyond plasma heating and current drive, encompassing numerous facets such as the management of MHD instability, plasma startup, and the regulation of wall conditions [2].

Ion cyclotron resonance heating schemes typically launch low-frequency radiofrequency waves from the low-field side to the high-field side, and the waves propagate into the plasma-heated region and then transfer the energy to the plasma through various absorption mechanisms. In the ion cyclotron frequency range, electrons absorb energy through Landau damping and transit-time magnetic pumping (TTMP) [5-6]. In some cases, the wave can be converted into an ionic Bernstein wave, which is called a mode conversion. Mode conversion can also directly heat the electrons, although it can be ignored in minority heating schemes in many tokamaks [7]. Instead, the ions, which are the main part of the energy absorption, absorb energy through cyclotron damping. When the frequency of the electromagnetic wave is similar to the ion cyclotron frequency, i.e., $\omega - k_{||}v_{||} = n\omega_{ci}$, there is a strong energy exchange between the wave and the ions. At present, there are two main heating schemes for ion cyclotron resonance heating. One is to heat the ions by the second harmonic absorption mechanism of the fast wave; the other is the minority heating scheme, i.e., the dispersive property is determined by the majority ions, and the resonance absorption is realized by minority ions. Ion cyclotron resonance heating not only has excellent heating of ions, but can also provide non-inductive current drive, control impurities, and reduce turbulent transport [8-11].

Computational programs based on plasma wave theory and dynamics are powerful tools for addressing thermal plasma problems. For example, the TORIC code employs spectral representation in the poloidal and toroidal directions [12-14], while the radial direction uses the finite element method (FEM); the AORSA code employs the Fourier coordinate method in all three directions [15]. These codes can fully account for spatial dispersion effects, thereby accurately describing the absorption process of ions at the fundamental and harmonic frequencies of the cyclotron frequency, as well as the linear mode conversion between fast and slow waves. They also cover the absorption process of electrons through Landau damping and the TTMP mechanism. However, due to the numerical solution schemes employed in the spectral representation

* Corresponding author: zlh_ustc@mail.ustc.edu.cn

method, these codes struggle to handle the scrape-off layer (SOL) at the plasma edge and complex geometric boundaries. Therefore, many core codes incorporating antenna structures and SOL have been proposed [16-20]. S. Shiraiwa provides a detailed summary of the progress made in the application of FEM in RF waves over the past decades [21]. In these programs, the models primarily utilize the thermal plasma dielectric tensor, employing the finite element method (FEM) to solve for given parallel and perpendicular wavenumbers (typically approximated using the fast-wave dispersion relation). Previously, we also carried out FEM simulation work on EAST ICRF heating. The simulation program integrates the edge and core plasmas [18]. This paper adopts a similar approach, but the perpendicular wavenumber is no longer approximated using the fast-wave dispersion relation; instead, it is obtained by iteratively solving the dispersion relation. The model integrates the antenna and plasma, with the simulation process self-consistently incorporating the antenna structure and thermal plasma-wave interaction, rather than the traditional simulation that only includes the plasma core region. By adjusting the plasma edge density and temperature distribution parameters, the influence of plasma parameters in the SOL region on wave propagation and absorption can be calculated, enabling the study of the interaction mechanism between the antenna and the plasma.

The main content of this paper is as follows: Section 1 is the introduction; Section 2 is the physical model and program settings; Section 3 is the simulation results and discussion; and finally, Section 4 is the conclusions.

2 Physical model and program settings

2.1 Wave equation and susceptibility tensor

This study employs a quasi-homogeneous approximation of the dielectric tensor, which requires prior knowledge of the parallel and perpendicular wave numbers. In most previous studies [16-18], the perpendicular wave number was approximated using a local fast-wave dispersion relation. In contrast, the parallel wave number was assumed to be constant or inversely proportional to the coordinate R. In this study, the parallel wavenumber is still assumed to be inversely proportional to R, while the perpendicular wavenumber is obtained by solving the dispersion relation in the absence of an external current density. The plasma geometry and response are assumed to be toroidal symmetric. Given a single toroidal mode number, we perform a Fourier decomposition in the toroidal direction to compute the wave field. Under these assumptions [22], the wave equation in a two-dimensional axisymmetric geometry is $\mathbf{M}\cdot\boldsymbol{E} = i\omega\mu_0\boldsymbol{J}_{ext}$, i.e.

$$\nabla\times\nabla\times\boldsymbol{E} - \frac{\omega^2}{c^2}\left[\mathbf{I}+\sum_j\boldsymbol{\chi}_j\right]\boldsymbol{E} = i\omega\mu_0\boldsymbol{J}_{ext}\ , \tag{1}$$

where $\boldsymbol{\chi}_j$ is the hot susceptibility tensor for species j, $\mathbf{I}$ is the identity matrix, $\boldsymbol{J}_{ext}$ is the external current density, ω is the angular frequency of ICRF antenna, and c is the light speed in vacuum. In cylindrical coordinates (R,ϕ,Z), the solution of the electric field can be written as

$$\boldsymbol{E}(R,\phi,Z) = \boldsymbol{E}(R,Z)e^{in_\phi\phi}\ , \tag{2}$$

where $\boldsymbol{E}$ is the complex amplitude and n_ϕ is the toroidal mode number.

We follow the Cartesian coordinates in Ref. [22] to describe the susceptibility tensor $\boldsymbol{\chi}_j$. In this coordinate system, the toroidal magnetic field is along the negative z-direction, and the wave vector is in the xoz plane, neglecting its y-direction component. The expression of $\boldsymbol{\chi}_j$ is (the specific form of $\chi_{n,j}$ can be found in Ref. [18]):

$$\boldsymbol{\chi}_j^{(Stix)}(k_x,k_z) = \begin{pmatrix} \chi_{1,j} & \chi_{2,j} & \chi_{4,j} \\ -\chi_{2,j} & \chi_{0,j}+\chi_{1,j} & -\chi_{5,j} \\ \chi_{4,j} & \chi_{5,j} & \chi_{3,j} \end{pmatrix}\ , \tag{3}$$

where all $\chi_{n,j}$ terms contain the parallel wave number k_z, while the perpendicular wave number k_x only appears in $\chi_{4,j}$ and $\chi_{5,j}$.

2.2 Coordinate system and assumptions about wavenumber

This work ignores the poloidal magnetic field and considers only the presence of a toroidal magnetic field, which usually does not have a large effect. That is because the poloidal field generally causes only an up- and downshift of the parallel wave number, which has little impact in the case of strong single-pass absorption [23-24]. The direction of the toroidal field is along the negative direction of z and the parallel wave number is given by

$$k_z = -\frac{n_\phi}{R}\ . \tag{4}$$

In previous studies, the solution of the perpendicular wave number k_x was generally considered to be simply the FW solution for cold plasma, i.e., $k_x = k_{x\_FW}$.

$$k_{x\_FW}^2 = \frac{\omega^2}{c^2}\left(S - n_{||}^2 - \frac{D^2}{S-n_{||}^2}\right)\ , \tag{5}$$

$$S = 1 - \sum_j \frac{\omega_{p,j}^2}{\omega^2-\Omega_{c,j}^2}\ , \tag{6}$$

$$D = \sum_j \frac{\omega_{p,j}^2}{\omega}\frac{\Omega_{c,j}}{\omega^2-\Omega_{c,j}^2}\ , \tag{7}$$

where $n_{||} = k_z c/\omega$ is parallel component of the refractive index. In this work, the perpendicular wave number is obtained by solving the dispersion relation, i.e., by solving $|\mathbf{M}| = 0$.

$$|\mathbf{M}| = \begin{vmatrix} k_z^2 - \frac{\omega^2}{c^2}(1+\sum_j\chi_{1,j}) & -\frac{\omega^2}{c^2}\sum_j\chi_{2,j} & -k_xk_z - \frac{\omega^2}{c^2}\sum_j\chi_{4,j} \\ \frac{\omega^2}{c^2}\sum_j\chi_{2,j} & k_x^2+k_z^2 - \frac{\omega^2}{c^2}[1+\sum_j(\chi_{0,j}+\chi_{1,j})] & \frac{\omega^2}{c^2}\sum_j\chi_{5,j} \\ -k_xk_z - \frac{\omega^2}{c^2}\sum_j\chi_{4,j} & -\frac{\omega^2}{c^2}\sum_j\chi_{5,j} & k_x^2+k_z^2 - \frac{\omega^2}{c^2}(1+\sum_j\chi_{3,j}) \end{vmatrix} = 0\ . \tag{8}$$

A MATLAB® code is used for the built-in fsolve function to iteratively solve for the distribution of k_x. According to the power law of k_x in Eq. (8), there should be two sets of solutions, corresponding to the fast wave solution and slow wave solution under EAST tokamak conditions. The fast wave solution is more meaningful because only it can propagate to the plasma core region. Therefore, we use the FW dispersion solution of the cold plasma as the initial value for the iterative solution process, converging to the fast wave solution under EAST tokamak conditions. After solving for k_x using an iterative method and substituting it into Eq. (3), the susceptibility tensor is obtained. Fig. 1

shows the difference between k_x obtained using this method and k_{x_FW} of cold plasma.

For the calculation of the dielectric tensor as well as the wave vector, we use the Cartesian coordinate system $(\boldsymbol{e}_x, \boldsymbol{e}_y, \boldsymbol{e}_z)$ mentioned in Ref. [22]. Here it is necessary to clarify the relationship between this coordinate system and the cylindrical coordinate system $(\boldsymbol{e}_R, \boldsymbol{e}_\phi, \boldsymbol{e}_Z)$ that we used for the calculation of the wave field. Where $\boldsymbol{e}_R$ is in the same direction as $\boldsymbol{e}_x$, $\boldsymbol{e}_\phi$ is inverse to $\boldsymbol{e}_z$, and $\boldsymbol{e}_Z$ is in the same direction as $\boldsymbol{e}_y$.

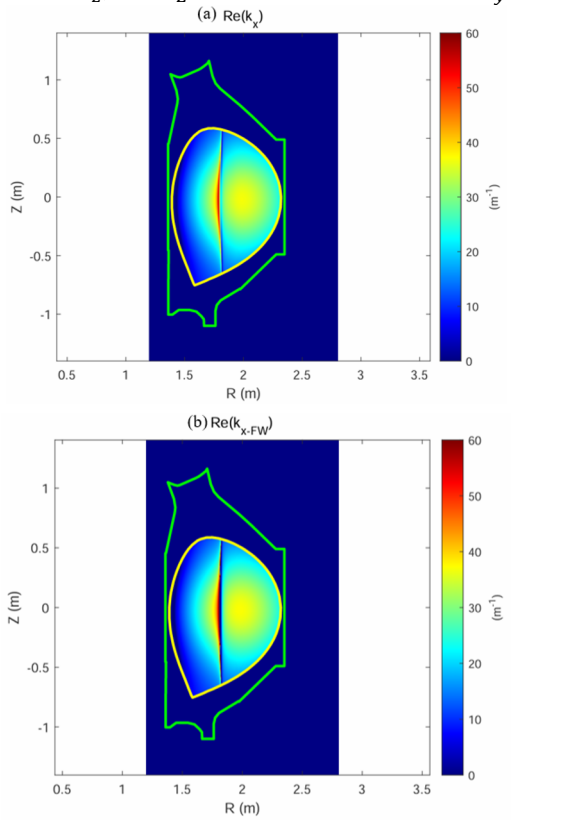

Fig. 1. The difference between k_x solved by the dispersion equation and k_{x_FW}, (a) k_x, (b) k_{x_FW}.

2.3 Power absorption

In the ion cyclotron resonance frequency range, power absorption is usually dominated by strong single-pass absorption so that reflected waves from the high-field side do not have a large impact on power absorption. In this paper, we consider the absorption mechanisms of electron damping, ion fundamental harmonic damping, and second harmonic damping, which are related to the anti-Hermitian part of the susceptibility tensor. Previous studies have similarly considered these absorption mechanisms and provided reasonable results [16-18, 23-24]. The local absorption of each component is given by

$$Q_j = \frac{\omega \varepsilon_0}{2} \Re[\boldsymbol{E}^* \cdot \boldsymbol{\chi}_j^A \cdot \boldsymbol{E}] \ . \tag{9}$$

Mode conversion is also an important absorption mechanism in ICRH, but this effect is not significant at low concentrations. This model can capture the confluence of fast waves and slow waves in the IIR layer. However, the effects of slow waves and ion-Bernstein waves at high temperatures are not considered in this paper.

2.4 Geometry, boundary condition and mesh configuration

The geometry of EAST includes the first wall, divertor, and antenna region. The antenna region comprises the antenna strip, Faraday screen, and barrier. The surfaces of the first wall and Faraday screen are assumed to be perfect electrical conductivity (PEC), i.e., $\boldsymbol{n} \times \boldsymbol{E} = 0$, where $\boldsymbol{n}$ is the unit normal vector. Since the plasma density in the antenna region is very small compared to the core region, we assume it to be a vacuum region. Following the previous assumptions, the model uses a cylindrical coordinate system (R, ϕ, Z), where R represents the radial direction, ϕ represents the magnetic field direction, and Z represents the vertical direction.

Fig. 2 shows the geometry of EAST. The first wall, divertor, and vacuum vessel are represented by black lines, while the antenna strip is represented by blue lines. The current density on the antenna surface is assumed to be

$$\boldsymbol{j}_k = \boldsymbol{t}_{ant} \tilde{J}_k e^{i\theta_k} \ , \tag{10}$$

where $\boldsymbol{t}_{ant}$ is the unit tangential vector on the antenna surface, $\tilde{J}_k$ is the amplitude of the current density intensity, and θ_k is the polar phase of the antenna, with k taking values of 1, 2. The Faraday screen is located between the vacuum vessel and the blue line and is not shown in Fig. 2. The boundary conditions for the Faraday screen are also PEC. The red line depicts the magnetic flux surfaces of equilibrium, with the outermost red line representing the last closed flux surface (LCFS). To match the actual parameters in the experiment, the plasma's major radius is 1.85 m, and the minor radius is 0.45 m.

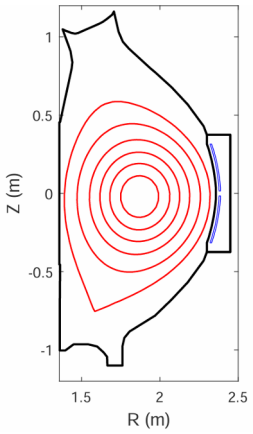

Fig. 2. Geometric shape of EAST (red represents the magnetic surface, blue represents the antenna; due to its small size, the Faraday screen is not shown).

As shown in Fig. 3, an unstructured triangular mesh was used in the simulation. Within the plasma core region, the mesh size ranged from 3 mm to 1 mm, while within the SOL, the typical mesh size ranged from 10 mm to 2 mm. Additionally, the mesh near the antenna band and Faraday screen in the vacuum region was refined. The model has 5×10^6 degrees of freedom and requires approximately 16 GB of RAM.

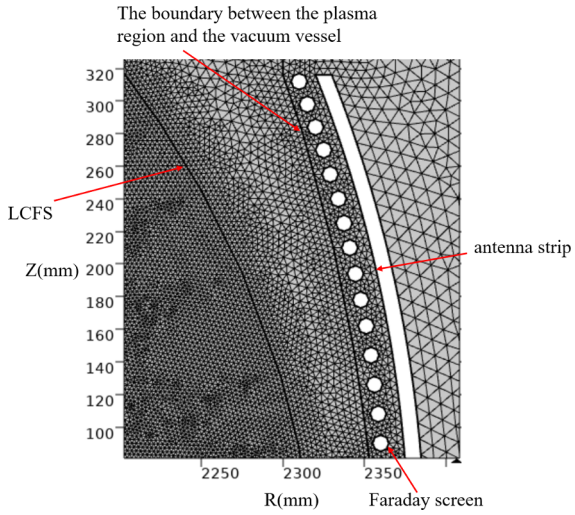

Fig. 3. Grid configuration.

2.5 Magnetic flux surfaces and parameter profiles

The flux function is employed to ascertain the temperature and density profiles. The flux function $\psi = \psi(R, Z)$ of the EAST equilibrium is analytically defined according to the magnetic surface literature [25]. The normalized flux ρ_{pol} is defined as

$$\rho_{pol} = \begin{cases} (\frac{\psi-\psi_0}{\psi_L-\psi_0})^{1/2} & inside\ LCFS \\ (1+|\frac{\psi-\psi_0}{\psi_L-\psi_0}|)^{1/2} & outside\ LCFS \end{cases}, \quad (11)$$

where ψ_0 and ψ_L are the magnetic flux values at the magnetic axis and LCFS, respectively.

The toroidal magnetic field B_t is assumed to be

$$B_t = \frac{B_0 R_0}{R}, \quad (12)$$

where B_0 is the magnetic induction intensity at the major radius R_0.

The electron density profile is defined as

$$n_e = \begin{cases} n_{e0} + (n_{eL} - n_{e0})\rho_{pol}^2 & inside\ LCFS \\ n_{emin} + (n_{eL} - n_{emin})\exp(-\frac{|\rho_{pol}-1|}{\lambda}) & outside\ LCFS \end{cases}, \quad (13)$$

where n_{e0} is the electron density at the magnetic axis, n_{eL} is the density at the LCFS, n_{emin} is the minimum density in the SOL region, and λ is the decay constant. With the electron density distribution, the ion density distribution can be obtained based on the ion concentration.

The temperature profile of electrons is defined as

$$T_e = \begin{cases} T_{e0} + (T_{eL} - T_{e0})\rho_{pol}^2 & inside\ LCFS \\ T_{emin} + (T_{eL} - T_{emin})\exp(-\frac{|\rho_{pol}-1|}{\kappa}) & outside\ LCFS \end{cases}, \quad (14)$$

where T_{e0} is the temperature of electrons at the magnetic axis, T_{eL} is the temperature at the LCFS, T_{emin} is the minimum temperature in the SOL region, κ is the decay constant, and the ion temperature profile is defined similarly.

3 Simulation results of D(H) minority heating

3.1 Comparison of simulation results for $\boldsymbol{\chi}_j(k_x, k_z)$ and $\boldsymbol{\chi}_j(k_{x\_FW}, k_z)$

As mentioned above, this paper derives the perpendicular wave number, k_x, by solving the dispersion relation in the absence of an external current density. To intuitively demonstrate the advantages of this method, we also calculated the results using k_{x_FW}, which is given by the fast wave dispersion relation. Below, we present the results calculated using the two susceptibility tensors, $\boldsymbol{\chi}_j(k_x, k_z)$ and $\boldsymbol{\chi}_j(k_{x\_FW}, k_z)$. The D(H) minority heating simulation parameters are shown in Table 1.

Table 1. D(H) minority heating simulation parameters.

Parameter	Value
ω	37 MHz
B_0	2.45 T
R_0	1.85 m
n_{e0}	$5 \times 10^{19}\mathrm{m}^{-3}$
n_{eL}	$1.5 \times 10^{19}\mathrm{m}^{-3}$
n_{emin}	$2 \times 10^{16}\mathrm{m}^{-3}$
T_{e0}	5 keV
T_{eL}	0.8 keV
T_{emin}	0.6 keV

Fig. 4 shows the calculation results of the left-handed electric field $\boldsymbol{E}_+$ under two $\boldsymbol{\chi}_j$ conditions. It can be seen that both simulate the phenomenon of fast waves reaching the ion-ion hybrid resonance layer (IIR layer). However, the electric field distribution calculated using $\boldsymbol{\chi}_j(k_x, k_z)$ is smoother (especially near the IIR layer). This may be related to the fact that the k_{x_FW} derived from the dispersion relation of fast waves does not consider the thermal effects of the IIR layer.

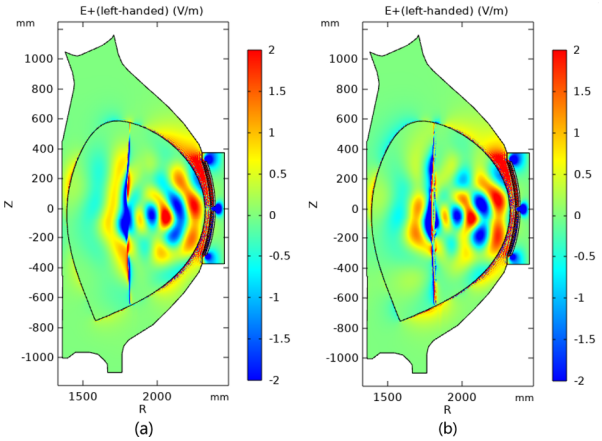

Fig. 4. Real part of $\boldsymbol{E}_+$ ($n_\phi = 18, X[H] = 5\%$) calculated by (a) $\boldsymbol{\chi}_j(k_x, k_z)$, (b) $\boldsymbol{\chi}_j(k_{x\_FW}, k_z)$.

Fig. 5 shows the calculation results of H ion power absorption under two $\boldsymbol{\chi}_j$ conditions. The shape and distribution of the H ion fundamental frequency absorption layer calculated using $\boldsymbol{\chi}_j(k_x, k_z)$ are more reasonable. The absorption distribution values calculated using $\boldsymbol{\chi}_j(k_{x\_FW}, k_z)$ are discontinuous (especially near the IIR layer) and have relatively large values.

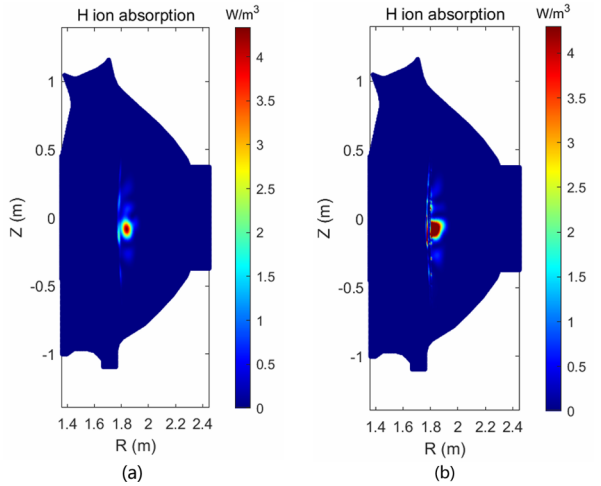

Fig. 5. H ion absorption ($n_\phi = 18, X[H] = 5\%$) calculated by (a) $\boldsymbol{\chi}_j(k_x, k_z)$, (b) $\boldsymbol{\chi}_j(k_{x\_FW}, k_z)$.

Fig. 6 shows the electron power absorption calculation results under two $\boldsymbol{\chi}_j$ conditions. It can be seen that the electron absorption distribution calculated using $\boldsymbol{\chi}_j(k_{x\_FW}, k_z)$ is mainly concentrated near the IIR layer. However, the electron absorption distribution calculated using $\boldsymbol{\chi}_j(k_x, k_z)$ is widely concentrated in the region with a stronger right-handed electric field $\boldsymbol{E}_-$, indicating that $\boldsymbol{\chi}_j(k_x, k_z)$ better considers FLR effects in the electron absorption mechanism.

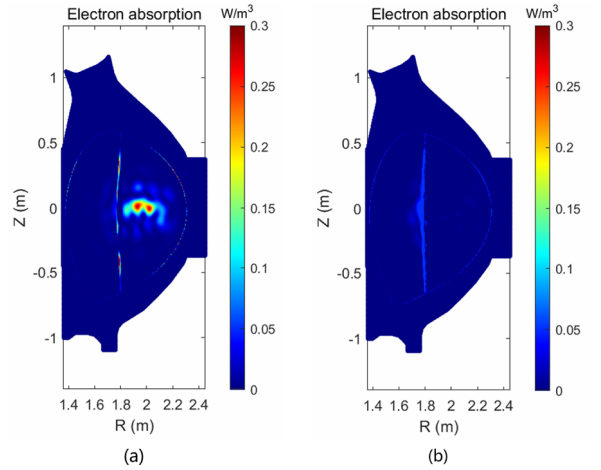

Fig. 6. Electron absorption ($n_\phi = 18, X[H] = 5\%$) calculated by (a) $\boldsymbol{\chi}_j(k_x, k_z)$, (b) $\boldsymbol{\chi}_j(k_{x\_FW}, k_z)$.

3.2 Power absorption for $\boldsymbol{\chi}_j(k_x, k_z)$

The functional relationship between the power absorption ratio of different components and n_ϕ is shown in Fig. 7. The absorption power of each component has been normalized according to the total absorption power of the plasma (including the SOL region). The power absorbed by H ions ranges from 60% to 90%, and overall, the power absorbed by H ions is greater than 75%. This confirms that the ion cyclotron resonance heating of a small number of H ions plays a dominant role in the simulation. However, at a given low n_ϕ, the power absorbed by D ions is significantly larger than the actual value, and there is currently no clear physical reason to explain this phenomenon. This may be due to numerical causes resulting from field convergence near the IIR layer in the SOL region and assumptions about the dispersion relation.

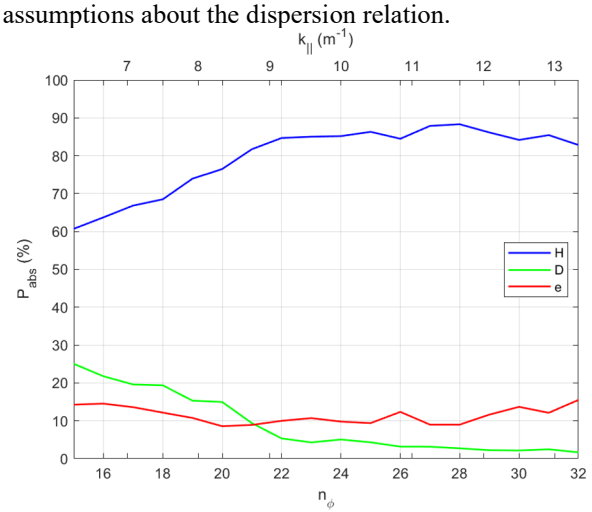

Fig. 7. Absorption ratio of each component when $X[H] = 5\%$.

The power density absorbed by each component of plasma is shown in Fig. 8. It can be seen that the total power absorption in the figure is similar to the H ion absorption profile. This also proves that in the simulation, the ion cyclotron resonance heating of a small number of H ions plays a dominant role, which is consistent with the results in Fig. 7. From the figure, the on-axis heating performance of H ions and D ions can be observed. Compared to the power absorption of H ions, the absorption of electrons and D ions is very weak.

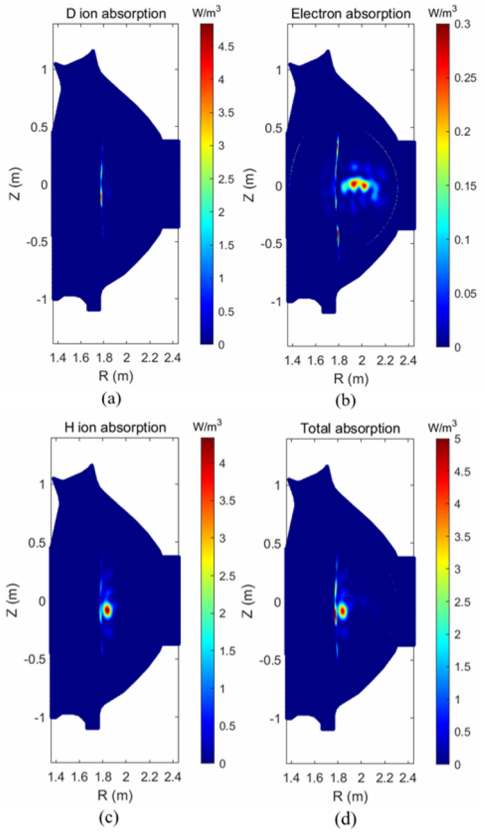

Fig. 8. Power absorption of each component ($n_\phi = 18, X[H] = 5\%$), (a) D ion absorption, (b) electron absorption, (c) H ion absorption, (d) total absorption.

4 Conclusions

The main focus of this paper is the development of the resolution of the perpendicular wavenumber based on a FEM code that integrates edge and core plasmas. By adjusting toroidal wave number, the propagation and absorption of ion cyclotron waves were calculated, and the interaction mechanism between the RF wave and plasma was investigated on EAST. The reflection and confluence of fast waves and slow waves near the IIR layer were observed in the simulation. The use of the modified k_x allows for more consistent calculation of wave propagation and yields power deposition results of each component that are more consistent with previous research findings.

The ICRF power deposition characteristics were also analyzed using this code. The ion cyclotron resonance heating of minority ions, such as H ions, plays a dominant role in the absorption process within the plasma core region. As can be clearly seen from Fig. 7, when n_ϕ(or $k_{||}$) is low, the power absorption ratio of H minority improves with increasing n_ϕ(or $k_{||}$). Calculations show that the power deposition area of electrons is broader and not limited to the IIR layer. However, this does not have a significant effect on total power absorption, as the proportion of power absorbed by electrons is very low. In the D(H) minority heating simulation, the power deposition in the SOL region plasma is only about 5%, which may be because more physical effects have not yet been added to the SOL region in this work. Based on these frameworks, new physical effects can be added in the next work to analyze and optimize heating schemes.

This work was supported by the National Key Research and Development Program of China (Nos. 2019YFE03070000 and 2019YFE03070003); National Natural Science Foundation of China (Nos. 11975265 and 11775258); Comprehensive Research Facility for Fusion Technology Program of China (No. 2018-000052-73-01-001228).

References

1. J. Adam, Review of tokamak plasma heating by wave damping in the ion cyclotron range of frequency, Plasma Phys. Control. Fusion. **29**, 443 (1987). https://doi.org/10.1088/0741-3335/29/4/001
2. J. Ongena et al., Recent advances in physics and technology of ion cyclotron resonance heating in view of future fusion reactors, Plasma Phys. Control. Fusion. **59,** 054002 (2017). https://doi.org/10.1088/1361-6587/aa5a62
3. X. J. Zhang et al., First results from H-mode plasmas generated by ICRF heating in the EAST, Nucl. Fusion. **53,** 023004 (2013). https://doi.org/10.1088/0029-5515/53/2/023004
4. J. R. Wilson and P. T. Bonoli, Progress on ion cyclotron range of frequencies heating physics and technology in support of the International Tokamak Experimental Reactor, Phys. Plasmas. **22** (2015). https://doi.org/10.1063/1.4901090
5. E. Ott, B. Hui and K. R. Chu, Theory of electron cyclotron resonance heating of tokamak plasmas, No. NRL-MR-4028. Naval Research Lab. (NRL), Washington, DC (United States), 1979
6. B. Lloyd, Overview of ECRH experimental results, Plasma Phys. Control. Fusion. **40**, A119 (1998). https://doi.org/10.1088/0741-3335/40/8A/010
7. B. Zaar et al., Iterative addition of parallel non-local effects to full wave ICRF finite element models in axisymmetric tokamak plasmas, Nucl. Fusion. **64,** 066017 (2024). https://doi.org/10.1088/1741-4326/ad3c51
8. E. Lerche et al. Optimization of ICRH for core impurity control in JET-ILW, Nucl. Fusion. **56**, 036022 (2016). https://doi.org/10.1088/0029-5515/56/3/036022
9. Y. O. Kazakov et al. Potential of ion cyclotron resonance frequency current drive via fast waves in DEMO, Plasma Phys. Control. Fusion. **57**, 025014 (2014). https://doi.org/10.1088/0741-3335/57/2/025014
10. F. J. Casson et al. Predictive multi-channel flux-driven modelling to optimise ICRH tungsten control and fusion performance in JET, Nucl. Fusion. **60**, 066029 (2020). https://doi.org/10.1088/1741-4326/ab833f
11. A. D. Siena et al., Electromagnetic turbulence suppression by energetic particle driven modes, Nucl. Fusion. **59**, 124001 (2019). https://doi.org/10.1088/1741-4326/ab4088
12. M. Brambilla, Modelling heating and current drive in the ion cyclotron frequency range, Plasma Phys. Control. Fusion. **35**, A141 (1993). https://doi.org/10.1088/0741-3335/35/SA/009
13. M. Brambilla, A note on the toroidal plasma dispersion function, Phys. Lett. A. **188**, 376 (1994). https://doi.org/10.1016/0375-9601(94)90479-0
14. M. Brambilla, Numerical simulation of ion cyclotron waves in tokamak plasmas, Plasma Phys. Control. Fusion. **41**, 1 (1999). https://doi.org/10.1088/0741-3335/41/1/002
15. E. F. Jaeger et al., Advances in full-wave modeling of radio frequency heated, multidimensional plasmas, Phys. Plasmas. **9**, 1873-1881 (2002). https://doi.org/10.1063/1.1455001
16. P. Vallejos et al. Effect of poloidal phasing on ion cyclotron resonance heating power absorption, Nucl. Fusion. **59**, 076022 (2019). https://doi.org/10.1088/1741-4326/ab1ab7
17. P. Vallejos et al., Iterative addition of finite Larmor radius effects to finite element models using wavelet decomposition, Plasma Phys. Control. Fusion. **62**, 045022 (2020). https://doi.org/10.1088/1361-6587/ab6f55

18. J. H. Zhang, X. J. Zhang and C. M. Qin. Finite elements method-based ICRF wave heating simulation integrating with SOL plasma for EAST tokamak, Nucl. Fusion. **62**, 076032 (2022). https://doi.org/10.1088/1741-4326/ac5451
19. L. Lu et al., Ion cyclotron wave coupling in the magnetized plasma edge of tokamaks: impact of a finite, inhomogeneous density inside the antenna box, Plasma Phys. Control. Fusion. **58**, 055001 (2016). https://doi.org/10.1088/0741-3335/58/5/055001
20. M. Usoltceva et al., Simulation of the ion cyclotron range of frequencies slow wave and the lower hybrid resonance in 3D in RAPLICASOL, Plasma Phys. Control. Fusion. **61**, 115011 (2019). https://doi.org/10.1088/1361-6587/ab476d
21. S. Shiraiwa, Finite element modeling of RF waves in fusion plasmas: progress in past decades and future role, 25th Topical Conference on Radio-Frequency Power in Plasmas, Schloss Hohenkammer, Germany, May 19-22 (2025). https://www.ipp.mpg.de/5534048
22. T. H. Stix, Waves in Plasmas (New York: American Institute of Physics, 1992)
23. E. F. Jaeger et al., All-orders spectral calculation of radio-frequency heating in two-dimensional toroidal plasmas, Phys. Plasmas. **8**, 1573 (2001). https://doi.org/10.1063/1.1359516
24. D. Van Eester, E. Lerche, and M. Evrard, A 2D finite element wave equation solver based on triangular base elements, AIP Conference Proceedings. **1187**, 597 (2009). https://doi.org/10.1063/1.3273822
25. A. J. Cerfon and J. P. Freidberg, “One size fits all” analytic solutions to the Grad–Shafranov equation, Phys. Plasmas **17**, 032502 (2010). https://doi.org/10.1063/1.3328818